

Efficient photocatalytic degradation of Rhodamine B dye using solar light-driven La Mn co-doped Fe2O3 nanoparticles

Sobia Maqbool

The Government Sadiq College Women University Bahawalpur

Adeel Ahmed (✉ Adeelchemist7@gmail.com)

Qingdao University

Arif Mukhtar

The Islamia University of Bahawalpur Pakistan

Muhammad Jamshaid

The Islamia University of Bahawalpur Pakistan

Aziz Ur Rehman

The Islamia University of Bahawalpur Pakistan

Saima Anjum

The Government Sadiq College Women University Bahawalpur

Research Article

Keywords: Solar-light, Photocatalyst, Degradation, Organic Pollutants, Rhodamine B, Doped Fe2O3

Posted Date: April 19th, 2022

DOI: <https://doi.org/10.21203/rs.3.rs-1462007/v1>

License:  This work is licensed under a Creative Commons Attribution 4.0 International License.

[Read Full License](#)

Abstract

This work aims to develop a highly efficient solar light-induced photocatalyst based on La \AA Mn co-doped Fe₂O₃ nanoparticles. Pure Fe₂O₃ and La \AA Mn co-doped Fe₂O₃ nanoparticles were fabricated by a simple co-precipitation method. The photocatalysts were analyzed for their morphological, structural, and magnetic characteristics. The photocatalytic performance of the Fe₂O₃, La_{0.1}Mn_{0.3}Fe_{1.60}O₃, and La_{0.2}Mn_{0.2}Fe_{1.60}O₃ catalysts was assessed by their capability to degrade Rhodamine B (RhB) under solar light illumination. La_{0.2}Mn_{0.2}Fe_{1.60}O₃ displayed exceptional degradation performance, degrading RhB to 91.78% in 240 min, in comparison to La_{0.1}Mn_{0.3}Fe_{1.60}O₃ (71.09%) and pristine Fe₂O₃ (58.21%) under specified reaction conditions [(RhB) = 50 ppm; (catalyst) = 40 mg/L; pH = 7; T = 25 °C]. The increased photocatalytic performance of La_{0.2}Mn_{0.2}Fe_{1.60}O₃ was attributed to the large surface area of the catalyst as a result of La \AA Mn co-doping. RhB degradation was affected by changing pH, catalytic dosage, dye concentration and temperature. The degradation of RhB was found to be pseudo-1st order kinetics. The photocatalyst material exhibited exceptional stability in four consecutive cyclic runs. The excellent photodegradation potential of La_{0.2}Mn_{0.2}Fe_{1.60}O₃ nanoparticles suggests that the effective eradication of organic pollutants can be achieved by these particles.

1. Introduction

From the past few years, it was found that the economy of the developed countries had been shifted from agriculture to industry due to a huge increase in the world's population (Zheng, Zhang, Meng, Wang, & Li, 2020). Although industrialization has provided ease in human life at the same time, it also cast a devastating impact on the environment by producing toxic and hazardous chemical species (Payra et al., 2019; Usman et al., 2021). Most of these industries discharge their toxic and stable chemical species into the wastewater, which ultimately damages aquatic life and human health (Lv et al., 2020; Steplin Paul Selvin et al., 2018). The wastewater contaminants are mostly organic dyes that are stable and toxic due to their complex and aromatic structures and are mostly waste-products of the tanneries, paint and textile industries (Ritika, Kaur, Umar, Mehta, & Kansal, 2019). Due to this stable nature, these organic pollutants are considered non-biodegradable. These pollutants cause serious environmental problems and human health issues, including skin and lungs destruction (Ashar et al., 2020; Das & Mahalingam, 2020). Many types of dyes, which are the most common organic pollutants, are produced in different industries and discharged into water bodies without proper treatment and are the major sources of water pollution (Ahmed et al., 2020; Chowdhury, Khan, Kumari, & Hussain, 2019; Khodadadi, Bordbar, & Nasrollahzadeh, 2017; Xu, Sun, Wang, Song, & Wang, 2018).

These water pollutants threaten human and aquatic life when discharged untreated into water bodies. These contaminants must be eradicated from the waste material before discharge into the water body. These contaminants are most commonly removed from wastewater by employing different methods. These methods include some electrochemical and physio-chemical techniques such as oxidation, chemical precipitation, adsorption, and microwave-assisted catalysis (Martínez-López et al., 2019;

Mostafa, Elsawy, Darwish, Hussein, & Abdaleem, 2020; Ndagijimana, Liu, Li, Yu, & Wang, 2019; Tang et al., 2020). These methods are very important and advantageous to remove the organic compounds from water, but there are various disadvantages and drawbacks associated with these methods. Due to environmental issues caused by above-mentioned methods, there was a need to develop an effective and eco-friendly technique to treat the harmful organic material (Bibi et al., 2017). The photocatalysis served the requisite properties, non-toxic, cost-effective and commercially easy to handle (Ahmed et al., 2019; Wu et al., 2020). In this technique, a photocatalyst is used to degrade the harmful organic materials in the presence of sunlight (Demirci, Yurddaskal, Dikici, & Sarioğlu, 2018; Raza et al., 2020). The active sites available on the surface of catalyst are responsible to absorb the sunlight and hence for the creation of active species to degrade harmful organic compounds (Gao et al., 2020; Kumar et al., 2020). For the last few years, metal oxide nanoparticles have been most commonly used as photocatalysts for the removal of toxic organic compounds from sewage water (Duan et al., 2020). These metallic nanoparticles have been fabricated by the use of different methods i.e., hydrothermal, sol-gel, co-precipitation and microwave-assisted techniques (Almeida, Rodembusch, Ferreira, & Caldas de Sousa, 2020; Dinesh, Pramod, & Chakma, 2020; Park & Ahn, 2020; Yousuf et al., 2019; Zare, Namratha, Thakur, & Byrappa, 2019; Zinatloo-Ajabshir, Salehi, & Salavati-Niasari, 2018). Although these fabrication methods are very effective and efficient for the production of nanoparticles, there are still some drawbacks of these methods, including high cost, requiring more energy, and producing harmful by-products (Liu et al., 2019; Rojas & Horcajada, 2020). It is required to choose a comparatively more effective, cheaper and least harmful technique for the fabrication of nanoparticles (Usman et al., 2019).

The solar light-sensitive metal oxide photocatalysts are very important for the decomposition of water pollutants. These metal oxides include CoO and CuO, which are light-sensitive (Lim, Chua, Lee, & Chi, 2014). Due to their variable oxidation state and active surface area, transition metal oxides have exhibited more vital activities. Iron oxide being transition metal oxide, have attained more consideration since the previous few years because of its outstanding uses in different fields. Iron oxides have been extensively used for photocatalysis (Bouhjar, Derbali, Mari', & Bessaï's, 2020). The Fe_2O_3 is an effective and advantageous photocatalyst to oxidize H_2O because of its environment-friendly potential. It absorbs a longer range of solar light, hence a more effective photocatalyst (W. Guo, Sun, Lv, Kong, & Wang, 2017). The photocatalytic activity of Fe_2O_3 nanoparticles has been found to be increased when treated with some other metals, more preferentially the transition metals. The Mn being cheaper, easily available, and environment-friendly properties, is the best transition metal used for doping of Fe_2O_3 nanoparticles (Chen et al., 2019). The doping of Fe_2O_3 with Mg also enhances the catalytic degradation of organic pollutants by generating more oxygen vacancies (Sun et al., 2020). The photocatalytic activity of Cr doped Fe_2O_3 nanorods was also found to be enhanced compared to undoped (Popov et al., 2021). The Ca doped Fe_2O_3 nanoparticles being cheaper and least harmful to the environment, were used preferably to degrade the RhB (an organic pollutant). The doping of Fe_2O_3 nanoparticles with Ca enhances electron transfer, so the degradation is increased by many folds (S. Guo et al., 2020). Ti@ Fe_2O_3 nanoparticles have been fabricated by using sol-gel technique. Doping by Ti significantly enhanced the surface area of Fe_2O_3 .

nanoparticles. It also enhanced reducibility and catalytic activity in oxidation of toluene (Abbas Khaleel, Maliha Parvin, Moahmmmed AlTabaji, & Al-zamly, 2018).

Co metal doping of Fe_2O_3 reduces its bandgap, and it also enhances photocatalytic activity because it acts as a trapping center for electrons. Co-doped Fe_2O_3 nano sized particles have shown a good photocatalytic performance to remove the hazardous industrial effluents (R. Suresh et al., 2017). Hydrothermally synthesized Mg-doped $\text{CuO}/\text{Fe}_2\text{O}_3$ was found to be a good catalyst for phenol degradation. The degradation rate of nanoparticles is enhanced by doping the material with Mg. This increase is due to the fact that OVs number is enhanced due to Mg doping in the catalysts (Mengying Sun, Yu Lei, Hao Cheng, Jianfeng Ma, Yong Qin, Yong Kong, et al., 2020). The chromium metal is used as dopant material because of its certain characteristic properties like ion donor and enhancement of charge carrier concentration in Fe_2O_3 sheets. Mainly the doping of Cr metal onto the iron oxide sheet enhances the conductance and charge transport in these sheets (Feriel Bouhjar, Lotfi Derbali, Bernabe Mari'a, & Bessais, 2020). The photocatalytic performance of $\text{CuS}/\text{Fe}_2\text{O}_3/\text{Mn}_2\text{O}_3$ nanomaterials was determined by the degradation of ciprofloxacin (CIP) (Yan Huang et al., 2020). By using the magnesium metal as dopant have also enhanced the photocatalytic activity of $\text{CuO}/\text{Fe}_2\text{O}_3$ to degrade the phenolic compounds (Mengying Sun, Yu Lei, Hao Cheng, Jianfeng Ma, Yong Qin, Kong, et al., 2020).

The doping with Cu enhanced its photoelectrochemical property. The co-doping further enhanced some characteristic properties of the Fe_2O_3 . Co-doping of the Fe_2O_3 with Si and Ti has increased its donor concentration. The co-doping of Fe_2O_3 with N and Zn has enhanced its concentration of acceptors and photo response (Reddy et al., 2019). It is observed that the doping of nanoparticles with Mn imparts various tremendous characteristics to them. The enhancement of photocatalytic performance of the Fe_2O_3 nanoparticles was also observed by doping with Mn. This doping has enhanced the photo-induced charges which in turn increased the capacity of the Fe_2O_3 nanoparticles to transfer the charges (N. Wang, Han, Wen, Liu, & Li, 2019). The nanoparticles having Mn doping also undergo agglomeration due to their higher surface energy. The photocatalytic effect was found to be further enhanced by the use of rare-earth metal ions in addition to Mn. These rare-earth metals are responsible for the inhibition of photo-induced electron-hole recombination (Rashmi et al., 2017). These rare earths also enhance the number of active sites which are responsible to degrade the harmful organic compounds by the creation of heterojunctions in the nanoparticles, which ultimately inhibits the electron-hole recombination (Harish, Bhojya Naik, Prashanth Kumar, & Viswanath, 2013). The rare-earth metals in combination with Mn are also responsible for changing the intrinsic properties of the nanoparticles due to the unique 4f-3d coupling of electrons. La is more preferable as compared to the other rare-earths due to its distinct properties such as larger size (1.6061 \AA), simple electronic spectra, reactivity, paramagnetic nature, higher resistivity ($615 \Omega\text{m}$) and lower melting point (920°C). La in combination with Mn have enhanced physical, chemical and catalytic properties of the nanoparticles (Baig et al., 2020; Peng, Fu, Yang, & Ouyang, 2016).

Because of these remarkable properties of cations of lanthanide series, in the present work, we have chosen La in combination with Mn for the co-doping of Fe_2O_3 nanoparticles to enhance the photocatalytic performance of these nanoparticles.

2. Experimental

2.1. Chemicals

The chemicals required for the fabrication of La@Mn co-doped Fe_2O_3 nanoparticles are listed here. $\text{Fe}(\text{NO}_3)_3 \cdot 9\text{H}_2\text{O}$ (Merck, 98%), $\text{Mn}(\text{NO}_3)_2 \cdot 4\text{H}_2\text{O}$ (Merck 98%), $\text{La}(\text{NO}_3)_3$, (Merck 98%), deionized water, sodium hydroxide [NaOH, Sigma, 98%], were utilized as precursors and reagents for this research work. The RhB an organic dye utilized during this work, was procured from Almadina chemicals. All these precursors and chemicals which were utilized in this research work were in highly purified form and were used as received from the supplier.

2.2. Fabrication of Fe_2O_3 nanoparticles

To fabricate the Fe_2O_3 nanoparticles, 20.2 g of $\text{Fe}(\text{NO}_3)_3 \cdot 9\text{H}_2\text{O}$ was dissolved in 250 ml of deionized water to prepare a 0.2M iron solution. Fe_2O_3 nanoparticles were synthesized by using the chemical co-precipitation route. During this particular procedure, $\text{Fe}(\text{NO}_3)_3 \cdot 9\text{H}_2\text{O}$ solution was stirred on the hotplate for 15 minutes at 60 °C temperature to get a homogeneous solution. At the start of this experiment pH of the solution was found to be 4, and the color was orange-yellow. Then solution pH was increased from 4 to 11 by the addition of 1M sodium hydroxide solution and was maintained at 11. After the maintenance of pH, the solution became blackish-green. Stirring was continued for 4hrs at 80 °C. The solution was cooled, and precipitates were separated. The washing of these precipitates was carried out by deionized water many times till the pH became neutral. These precipitates were then dried in an oven at 150–200 °C and annealed at 450 °C for 4hrs in a furnace to get the final product.

2.3. Preparation of La@Mn co-doped Fe_2O_3 nanoparticles

For the preparation of La@Mn co-doped Fe_2O_3 nanoparticles, different molar concentrations of solutions were made such as ferric nitrate (0.16M), manganese nitrate (0.03M, 0.02M) and lanthanum nitrate (0.01M, 0.02M) were made by the addition of specific quantities of these salts in water separately. Briefly, 16.6 g of ferric nitrate was added in 250 ml of deionized water and was stirred for 15 minutes at 60 °C to get a homogeneous solution. 0.02M solution of manganese nitrate was added to the above solution at the same temperature with constant stirring for 15 minutes. After this, 0.02M solution of lanthanum nitrate was added drop wise while it was also stirred continuously. At the start of this experiment pH of the solution was found to be 4, and the color was orange-yellow. Then solution pH was increased from 4 to 11 by the addition of 1M sodium hydroxide solution and was maintained at 11. Stirring was continued for 4hrs at 80 °C. Then the solution was cooled, and precipitates were separated. The washing of these precipitates was carried out by deionized water many times till the pH became neutral. The precipitates

were then dried in an oven at 150–200 °C and annealed at 450 °C for 4hrs in a furnace to get the final product. The schematic representation for the synthesis of La_xMn co-doped Fe₂O₃ nanoparticles is presented in Fig. 1.

2.4. Characterization

The morphology and particle size of undoped Fe₂O₃ and La_xMn co-doped Fe₂O₃ nanoparticles was examined by using Scanning Electron Microscope (SEM, Hitachi SX-650). Similarly, the TEM is used for the visualization and determination of morphological properties of nanoparticles. The FTIR spectrometer (Nikolet Nexus-470) was used for taking the spectra of the fabricated doped and undoped nanoparticles in the 400–3000 cm⁻¹ wavelength range. The X-ray analysis of the prepared nanoparticles was performed to determine the nanoparticles' purity and crystallinity. The Dynamic light scattering analysis was performed using NANO ZS Malvern Zetasizer for the measurement of zeta potential and particle size distribution. The magnetic properties of as fabricated particles were determined by the use of a magnetic field of -15000 to +15000 Oe strength. The nitrogen adsorption-desorption on the surface of nanoparticles and subsequently plotting a BET isotherm was utilized to measure the surface area of as fabricated particles. This analysis was performed by using Micrometrics Physisorption Analyzer (ASAP 2020). The UV spectrophotometer (Perkin Elmer, USA) was used for the measurement of photocatalytic performance of the as-prepared nanoparticles in the region of 200–700 nm.

2.5. Photocatalytic activity

The photocatalytic efficiency of pure Fe₂O₃ and La_xMn co-doped Fe₂O₃ nanoparticles was assessed by the degradation of RhB dye under solar light illumination. In a conventional degradation procedure, 40 mg/L of catalyst was mixed with 100 mL of RhB (50 ppm) in ultrapure water. To achieve the adsorption-desorption equilibrium, the resulting mixture were put in the dark and continuously agitated for 30 minutes. Following that, the mixture was illuminated with solar light, and 1 mL sample was taken at fixed time intervals and centrifuged at 5000 rpm to remove the residual catalyst particles. A UV-Vis spectrophotometer was used to check the concentration of RhB dye (Eq. 1).

$$\text{Degradation(}\%) = \frac{(C_0 - C)}{C_0} \times 100(1)$$

C₀ = Initial concentration of RhB dye, C = Dye concentration at time t.

The photocatalytic effect of the La_{0.2}Mn_{0.2}Fe_{1.6}O₃ nanoparticles was further studied at different experimental conditions.

3. Result And Discussion

3.1. SEM analysis

The shape and particle size of undoped Fe_2O_3 and La-Mn co-doped Fe_2O_3 nanoparticles was examined by using SEM analysis. The SEM micrographs of Fe_2O_3 nanoparticles have shown that the fabricated nanoparticles appeared as semi-spherical shaped with small aggregations in clusters and different sizes as shown in Fig. 2a.

The bimetallic doping of these Fe_2O_3 nanoparticles with La and Mn in different compositions affected the size of particles to a measurable extent. The morphology of the doped nanoparticles was not affected significantly due to this bimetallic doping. As the size of dopant metal ion Mn^{+2} is not much different from parent Fe^{+3} ions, so its doping does not affect the size of doped nanoparticles greatly. The size of the La^{+3} is much bigger (1.6061 Å) as compared to Mn^{2+} (0.83 Å) and Fe^{3+} (0.63 Å) ions present in parent nanoparticles. These larger La ions induce lattice imperfections and also lattice strain. Based on this reason the particle size of as fabricated doped nanoparticles was found to be reduced by increasing the molar concentration of lanthanum ions. The micrographs of the doped nanoparticles at different concentrations of Mn and La metals were taken.

Figure 2b shows the micrograph of $\text{La}_{0.1}\text{Mn}_{0.3}\text{Fe}_{1.6}\text{O}_3$, and reduction in size of doped particles was observed in comparison to the undoped Fe_2O_3 nanoparticles. Similarly, Fig. 2c shows the micrograph of $\text{La}_{0.2}\text{Mn}_{0.2}\text{Fe}_{1.6}\text{O}_3$ nanoparticles. These micrographs have shown a reduction in the size of the particles that take place by increasing the dopant La metal ions. Due to this reduction in the sizes of as fabricated doped nanoparticles, the active surface of the particles is increased, so the catalytic performance of these particles is also enhanced (Ahmed, Usman, Wang, et al., 2021).

3.2. TEM analysis

TEM analysis was performed to visualize and determine the morphological properties of nanoparticles as presented in Fig. 3. The doping of Fe_2O_3 nanoparticles has resulted in aggregation of the particles, which in turn produced inter-particle mesopores resulting in enhancement of the surface area. It was observed from TEM micrographs of Fe_2O_3 given in Fig. 3a that the average size as calculated by Nanomeasure software was found to be 48.137 nm, while the doping of Fe_2O_3 with La and Mn reduces the size of these particles. Figure 3b shows the micrograph of $\text{La}_{0.1}\text{Mn}_{0.3}\text{Fe}_{1.6}\text{O}_3$ nanoparticles, size of these particles was found to be 46.923 nm. Similarly, Fig. 3c shows the micrograph of $\text{La}_{0.2}\text{Mn}_{0.2}\text{Fe}_{1.6}\text{O}_3$ nanoparticles, and also their size was estimated to be 42.861 nm. The morphology of all the samples was found to be semi-spherical shaped, which is indication of the fact that morphology of particles is not significantly changed, but only the size of the particle is affected.

3.3. FTIR analysis

The FTIR spectra of the prepared nanoparticles (undoped and doped) were taken to determine structural parameters. The spectra of nanoparticles have shown two absorption peaks in 400–3000 cm^{-1} region for metal-oxygen stretching vibrations. Out of these two prominent absorption peaks, one observed in the low frequency region (400–500 cm^{-1}) for octahedral M-O stretching vibrations. Similarly, the peak at a

higher frequency region ($500\text{--}600\text{ cm}^{-1}$) appeared because of tetrahedral stretching vibrations (Ahmed, Usman, Wang, et al., 2021). The FTIR spectra for all three types of nanoparticles were taken and are represented in Fig. 4.

The spectra for Fe_2O_3 , $\text{La}_{0.1}\text{Mn}_{0.3}\text{Fe}_{1.6}\text{O}_3$ and $\text{La}_{0.2}\text{Mn}_{0.2}\text{Fe}_{1.6}\text{O}_3$ nanoparticles have shown that there is a small shift of absorption peak to the higher frequency region by the increase of concentration of dopant metal La. It is because of enhancement of large-sized La metal ions concentration, a decrease in particle size is observed, causing a decrease in bond length, which in turn causes the increase in the absorption frequency of the stretching bands. Due to this fact, a change in the position of the absorption band takes place, as shown in Fig. 4.

3.4. XRD analysis

The XRD analysis of the undoped Fe_2O_3 and La-Mn co-doped Fe_2O_3 nanoparticles was performed for the determination of purity and crystallinity of the nanoparticles. The analysis of these nanoparticles had confirmed the hexagonal geometry of the synthesized nanoparticles. The XRD results are shown in Fig. 5. According to these results, there are sharp and intense diffraction peaks at 2θ values, 24.13° (012), 33.15° (104), 35.61° (110), 40.85° (113), 49.47° (024), 54.08° (116), 57.58° (018), 62.44° (214), 63.98° (300), 72.26° (019), and 75.42° (220) respectively. These all the values of the peaks were compared with a standard pattern of Fe_2O_3 having hexagonal geometry. These XRD results found to be greatly comparable to the standard reference (JCPDS card no. 33–0664), which confirmed the synthesis of Fe_2O_3 (Ma & Chen, 2018). As there were no other irrelevant peaks observed in this result, which is the confirmation for the purity of as-synthesized nanoparticles. It was also found that the decrease in intensity of the peaks was observed for the La and Mn-doped nanoparticles. The peaks were also shifted due to this doping, and the shifting was increased by increasing the La ions concentration.

The crystal size of the synthesized Fe_2O_3 , $\text{La}_{0.1}\text{Mn}_{0.3}\text{Fe}_{1.6}\text{O}_3$ and $\text{La}_{0.2}\text{Mn}_{0.2}\text{Fe}_{1.6}\text{O}_3$ nanoparticles was calculated by using Debye Scherrer equation and measured to be 59.143, 58.237 and 51.948 nm, respectively.

These results have shown that the size of crystals is decreased by increasing the concentration of dopant metal La. This decrease in size of the doped nanoparticles is explained by the fact that the insertion of large-sized (1.6061 \AA) La^{3+} ions into the small-sized (0.63 \AA) Iron Fe^{3+} ions caused an increase in constant lattice value, which in turn decreases the crystallite size (Ahmad, Shah, Ashiq, & Khan, 2016).

3.5. DLS analysis

The DLS technique is utilized to measure the zeta potential and particle size distribution. The results plotted in Fig. 6 have shown a regular reduction in average size of particles due to the insertion of Mn and La ions in different compositions. The size of as fabricated Fe_2O_3 particles measured by DLS is 68.31 nm, as presented in Fig. 6a. Similarly, the size of the particles is reduced after bimetallic doping in a composition of $\text{La}_{0.1}\text{Mn}_{0.3}\text{Fe}_{1.6}\text{O}_3$. In this case, the average size is 67.42 nm, shown in Fig. 6b. The

average size of nanoparticles is further decreased to 57.28 nm when the concentration of dopant metal La is further increased in $\text{La}_{0.2}\text{Mn}_{0.2}\text{Fe}_{1.6}\text{O}_3$, as presented in Fig. 6c.

3.6. Magnetic properties

The magnetic properties of the nanoparticles were measured at standard conditions of temperature and pressure with a field strength of -15000 to + 15000 Oe. The M-H curves are used for the measurement of various magnetic parameters. The magnetic hysteresis curves for Fe_2O_3 nanoparticles and La-Mn co-doped Fe_2O_3 nanoparticles with different dopant concentrations $\text{La}_{0.1}\text{Mn}_{0.3}\text{Fe}_{1.6}\text{O}_3$ and $\text{La}_{0.2}\text{Mn}_{0.2}\text{Fe}_{1.6}\text{O}_3$ are given in Fig. 7. These M-H curves are used for the measurement of various magnetic properties i.e., M_s , H_c , M_r and squareness ratio. The values for Fe_2O_3 nanoparticles and La-Mn co-doped Fe_2O_3 nanoparticles as measured by using the M-H curves are given in Table 1.

These magnetic properties of as-synthesized undoped and doped nanoparticles are greatly influenced by various factors such as surface charge, cation stoichiometry, cation distribution, size of particles and the method of fabrication used (Sharifi, Shokrollahi, & Amiri, 2012). The results presented in Table 1 shows that the value of saturation magnetization (M_s) is decreased for the doped nanoparticles compared to undoped particles. The values for Fe_2O_3 nanoparticles is 6.17 emu/g while for $\text{La}_{0.1}\text{Mn}_{0.3}\text{Fe}_{1.6}\text{O}_3$ particles 3.73 emu/g and also for $\text{La}_{0.2}\text{Mn}_{0.2}\text{Fe}_{1.6}\text{O}_3$ is 2.89 emu/g. It is observed that the values are further decreased by increasing the concentration of the La^{+3} ion. The values of remanent magnetization also reduced similarly, Fe_2O_3 nanoparticles have M_r 1.15 emu/g, which is decreased to 0.68 emu/g for $\text{La}_{0.1}\text{Mn}_{0.3}\text{Fe}_{1.6}\text{O}_3$ particles and was further reduced by increasing the dopant ions concentration up to 0.52 emu/g for $\text{La}_{0.2}\text{Mn}_{0.2}\text{Fe}_{1.6}\text{O}_3$. The values for coercivity and squareness ratio are also affected in a similar way, but there is very little change for these parameters.

Table 1
Room temperature measurement of saturation magnetization (M_s), remanent magnetization (M_r), coercivity (H_c), and squareness ratio (M_r/M_s) of nanoparticles.

Composition	Saturation magnetization, M_s (emu/g)	Remanent magnetization, M_r (emu/g)	Coercivity, H_c (Oe)	Squareness ratio, M_r/M_s
Fe_2O_3	6.17	1.15	756.72	0.186
$\text{La}_{0.1}\text{Mn}_{0.3}\text{Fe}_{1.6}\text{O}_3$	3.73	0.68	756.69	0.182
$\text{La}_{0.2}\text{Mn}_{0.2}\text{Fe}_{1.6}\text{O}_3$	2.89	0.52	756.67	0.180

The decrease in the values of magnetic parameters is considered due to the insertion of La^{+3} ion into the Fe_2O_3 nanoparticle sublayers, which decreases the crystallinity and uniform morphology of the undoped Fe_2O_3 nanoparticle. These decreasing trends of magnetic parameters are also explained based on cation occupancy on the lattice sites, magnetic moment and the ionic radius. These above results are the basis

for the separation of doped and undoped nanoparticles, and thus these materials act as efficient photocatalysts in aqueous environment.

3.7. BET analysis

When BET analysis was performed for Fe_2O_3 nanoparticles, it was found that a type IV isotherm was formed, as shown in Fig. 8a. The surface area of Fe_2O_3 nanoparticles as calculated was $77.93 \text{ m}^2/\text{g}$. Similarly, the surface area of the $\text{La}_{0.1}\text{Mn}_{0.3}\text{Fe}_{1.6}\text{O}_3$ and also for $\text{La}_{0.2}\text{Mn}_{0.2}\text{Fe}_{1.6}\text{O}_3$ was also measured. It was observed that the surface area of $\text{La}_{0.1}\text{Mn}_{0.3}\text{Fe}_{1.6}\text{O}_3$ was found to be $80.23 \text{ m}^2/\text{g}$, as shown in Fig. 8b. Further analysis of the $\text{La}_{0.2}\text{Mn}_{0.2}\text{Fe}_{1.6}\text{O}_3$ nanoparticles has shown that by changing the molar concentrations of the dopant metals, the surface properties of these nanoparticles also changed, given in Fig. 8c. Also, for $\text{La}_{0.2}\text{Mn}_{0.2}\text{Fe}_{1.6}\text{O}_3$ was found to be $87.45 \text{ m}^2/\text{g}$.

From the above results, it is concluded that the surface area of the La-Mn co-doped Fe_2O_3 nanoparticles is increased by increasing the dopant concentrations. Due to this fact, the interaction between gas molecules and the nanomaterials is increased, which in turn also increases the adsorption-desorption (Zhou et al., 2016). This increased interaction between gas and nanomaterials will enhance the gaseous diffusion into the inner layers of the material having active sites (T. Wang et al., 2018). This whole process caused an enhancement in the photocatalysis of doped nanoparticles. This increased surface area is also beneficial to degrade the harmful organic compound.

3.8. Photocatalytic activity

The UV spectrophotometer is used for the measurement of photocatalytic performance of the as-prepared Fe_2O_3 nanoparticles and La-Mn co-doped Fe_2O_3 nanoparticles. This experiment was performed by calculating the degradation of RhB dye under sunlight. The dye solution was prepared and kept in dark to avoid any disturbance before applying catalyst. The dye solution and the catalyst solution were then mixed in the dark and kept for some time to attain the equilibrium. This mixture was irradiated by keeping under sunlight.

The degradation rate of dye was monitored by taking the samples from time to time and measuring the concentration by using a UV spectrophotometer. The decrease in dye concentration was detected with the increase in time, and ultimately, the dye concentration has almost vanished after 240 minutes. It is due to the fact that the nanoparticles acted as catalysts to degrade the dye molecules. These results of RhB degradation have shown 58.21% degradation by using Fe_2O_3 as represented in Fig. 9a. After the doping of Fe_2O_3 with Mn and La in the composition of $\text{La}_{0.1}\text{Mn}_{0.3}\text{Fe}_{1.6}\text{O}_3$, the degradation of dye was found to be increased to 71.09%, which is much higher than undoped nanoparticles, as represented in Fig. 9b. The results have shown that with the increase in concentration of dopant metal La, the percentage degradation of the RhB was also increased, as shown in Fig. 9c. It is evident that when the La concentration is increased to $\text{La}_{0.2}\text{Mn}_{0.2}\text{Fe}_{1.6}\text{O}_3$ dye degradation was also increased up to 91.78%.

Based on the above discussion, it is concluded that degradation rate is increased by doping and is further increased by increasing the composition of large-sized La^{+3} cation due to reduction in size and increase in surface area of the doped nanoparticles. The photocatalytic activity of $\text{La}_{0.2}\text{Mn}_{0.2}\text{Fe}_{1.6}\text{O}_3$ nanoparticles is further studied under different experimental conditions.

3.8.1. Effect of pH

As it is evident from the above discussion that degradation of RhB is best carried out by $\text{La}_{0.2}\text{Mn}_{0.2}\text{Fe}_{1.6}\text{O}_3$ nanoparticles. Further studies were also carried out to explore the effect of other factors on degradation process. Amongst these factors the pH of solution is considered as a very important and most noticeable dynamic factor to affect the degradation. This factor is responsible for the development of charge on catalyst surface, either positive or negative. Due to this reason of charge development, the adsorption rate of dye on the catalyst surface is also changed. In addition to the charge development, the size and aggregation of the catalyst is also affected by the change of pH, which in turn influences the degradation of dye (Ahmed, Usman, Yu, Gao, et al., 2021). In this experiment, a fixed amount of catalyst (40 mg/L) and that of dye (50 ppm) is used at a fixed temperature of 25 °C, and the pH of the solution is varied from 4 to 10. The pH of different solutions is maintained between 4 to 10 by the addition of hydrochloric acid and sodium hydroxide.

These dye solutions having different pH values were then exposed to sunlight, and degradation was calculated. To determine the effect of pH on degradation, the Zeta potential was used for the measurement of surface charge of the catalyst, as shown in Fig. 10. The point of zero potential (also known as IEP) was measured from Zeta potential values. The point of zero potential for $\text{La}_{0.2}\text{Mn}_{0.2}\text{Fe}_{1.6}\text{O}_3$ nanoparticle was found to be 8.46, as shown in Fig. 10. The catalyst surface attains positive charge when the solution's pH was decreased below 8.46, and the surface became negative by increasing the pH above 8.46.

As RhB is a cationic dye which means its attachment and also degradation, is favored at the pH value above 8.46 because above this point, the catalytic surface becomes negative. This negative surface attracts the cationic dye; hence degradation of dye is increased. Similarly, when the pH of the solution is decreased, a positive charge on the catalytic surface will be developed. This positive charge ultimately repels the cationic dye hence the degradation of dye is decreased with the decrease in pH of the solution. Due to this reason, the minimum degradation value of 43.3% was observed at pH 4. An increase in degradation of dye was observed with the enhancement of pH, and a maximum degradation of 89.34% was observed at pH 10 as represented in Fig. 11 and also in Table 2.

The kinetics of degradation of RhB dye have shown pseudo-first-order reaction as observed for different initial concentrations of dye solution. It is evident from above results that rate constant is increased from 0.0025 to 0.0092 min⁻¹ by varying the pH 4 to 10. Similarly, the regression coefficient values also increase from 0.9802 to 0.9960, which is in good agreement with the degradation percentage and are also according to the Langmuir Hinshelwood model of kinetics for pseudo first order.

Table 2

The pseudo-first-order kinetic parameters for RhB degradation under different pH conditions using $\text{La}_{0.2}\text{Mn}_{0.2}\text{Fe}_{1.6}\text{O}_3$ catalysts.

Catalyst	pH	Degradation (%)	$k(\text{min}^{-1})$	R^2
	4	43.30	0.0025	0.9802
	5	54.11	0.0031	0.9901
$\text{La}_{0.2}\text{Mn}_{0.2}\text{Fe}_{1.6}\text{O}_3$	6	60.58	0.0038	0.9830
	7	67.22	0.0043	0.9824
	8	72.47	0.0052	0.9915
	9	79.43	0.0064	0.9968
	10	89.34	0.0092	0.9960

3.8.2. Effect of catalytic dosage

The degradation rate was also significantly affected with the change in catalytic dosage. The catalytic dosage is also an important factor for the degradation of dyes because it also causes a change in surface area. The rate of reaction is influenced by this increase of surface area. The effect of photocatalyst $\text{La}_{0.2}\text{Mn}_{0.2}\text{Fe}_{1.6}\text{O}_3$ on photodegradation of RhB was observed using the different amounts 10, 20, 30, 40 and 50 mg/L while keeping other factors constant at the dye concentration 50 ppm, temperature 25 °C and the pH at 7 as shown in Fig. 12 and Table 3. These experimental results have shown that the dye degradation is increased as the catalytic dosage is enhanced by 10 to 50 mg/L. The minimum degradation of dye was found at a lower catalytic dosage of 10 mg/L, which was 60.49 and went on increasing by an increase of catalytic dosage up to 50 mg/L, which shows maximum photodegradation efficiency of the photocatalyst $\text{La}_{0.2}\text{Mn}_{0.2}\text{Fe}_{1.6}\text{O}_3$ as 90.07% at 25 °C, 50 ppm dye concentration and pH of the solution was maintained at 7.

This increase in photodegradation is due to an increase of surface area which in turn increases the active sites, due to this reason the rate of degradation is also increased by increasing catalytic amount. There will be an increased absorption of photons with the increase of surface area, which further increases the interfacial interaction among catalytic surface and dye molecules (Ahmed, Usman, Yu, Shen, & Cong, 2021).

The kinetics of degradation of RhB dye have shown pseudo-first-order reaction as studied under different catalytic dosages. The results have shown that the value of the rate constant is increased by 0.0037 to 0.0092 min^{-1} as the catalytic dosage is increased by 10 to 50 mg/L. Similarly, the values of the regression coefficient also increase from 0.9830 to 0.9961, which is in good agreement with the degradation percentage and are also according to the Langmuir Hinshelwood model of kinetics for pseudo first order.

Table 3
The pseudo-first-order kinetic parameters for RhB degradation at different catalyst dosage using $\text{La}_{0.2}\text{Mn}_{0.2}\text{Fe}_{1.6}\text{O}_3$ catalysts.

Catalyst	Catalyst dosage (mg/L)	Degradation (%)	$k(\text{min}^{-1})$	R^2
$\text{La}_{0.2}\text{Mn}_{0.2}\text{Fe}_{1.6}\text{O}_3$	10	60.49	0.0037	0.9830
	20	67.13	0.0042	0.9824
	30	72.57	0.0051	0.9915
	40	79.12	0.0064	0.9968
	50	90.07	0.0092	0.9961

3.8.3. Effect of dye concentration

The rate for the degradation of organic dyes is also greatly affected by the change in dye's concentration. The experiments have shown an increase in rate of reaction by increasing the concentration of dye. The effect of photocatalyst $\text{La}_{0.2}\text{Mn}_{0.2}\text{Fe}_{1.6}\text{O}_3$ on photodegradation of RhB was observed by using the various dye concentrations, i.e., 10, 20, 30, 40, 50 and 60 ppm while keeping other factors constant at the catalytic dosage 40 mg/L, temperature 25 °C and the pH at 7 as shown in Fig. 13 and Table 4.

The results have shown an increase in photocatalytic performance of $\text{La}_{0.2}\text{Mn}_{0.2}\text{Fe}_{1.6}\text{O}_3$ from 46.19–89.82% as the dye concentration was increased from 10 to 50 ppm while keeping other factors constant as 25 °C temperature, 40 mg/L catalytic dosage and pH 7. The results have also shown that by further increasing the dye amount the rate of degradation is reduced. It is because the active sites are available to a particular limit. But when amount of dye is further increased, there are not sufficient active sites available for the attachment of molecules (Ahmed et al., 2020). Therefore, the decrease in degradation of dye is observed, presented in Fig. 13.

The kinetics of degradation of RhB dye have shown pseudo-first-order reaction as studied under different amounts of dye. These results have shown that rate constant is increased from 0.0023 min^{-1} with the increase of dye concentration by 10 to 50 ppm. Similarly, regression coefficient is also increased from 0.9664 to 0.9974 min^{-1} , which is in good agreement with the degradation percentage and are also according to the Langmuir Hinshelwood model of kinetics for pseudo first order.

Table 4

The pseudo-first-order kinetic parameters for RhB degradation at different initial dye concentrations using $\text{La}_{0.2}\text{Mn}_{0.2}\text{Fe}_{1.6}\text{O}_3$ catalysts.

Catalyst	Dye Conc. (ppm)	Degradation (%)	$k(\text{min}^{-1})$	R^2
$\text{La}_{0.2}\text{Mn}_{0.2}\text{Fe}_{1.6}\text{O}_3$	10	46.19	0.0023	0.9664
	20	63.92	0.0039	0.9912
	30	72.13	0.0053	0.9947
	40	79.98	0.0064	0.9972
	50	89.82	0.0093	0.9974
	60	86.42	0.0078	0.9940

3.8.4. Effect of temperature

The rate of photodegradation of organic pollutants is affected by the change in temperature because the degradation of dyes is either endothermic or exothermic reactions. As it is one of the major factors, so the dye degradation is much affected by changing the temperature. The photodegradation of RhB is an endothermic reaction and is favored by the increase in temperature [21].

As it was found that the temperature has a very small effect on the degradation of dye, there is still an optimum temperature at which degradation of dye is maximum. For RhB, by using photocatalyst $\text{La}_{0.2}\text{Mn}_{0.2}\text{Fe}_{1.6}\text{O}_3$ the experiment was performed at different temperatures (25, 35, 45 and 55 °C) by keeping other factors, catalytic dosage (40 mg/L), pH 7 and concentration of dye (50 ppm) constant. The experimental results shown in Fig. 14 and Table 5 reveal that dye was degraded maximum up to 94.87% at 45 °C. These are the optimum conditions for this degradation experiment.

Table 5

The pseudo-first-order kinetic parameters for RhB degradation under different temperature conditions using $\text{La}_{0.2}\text{Mn}_{0.2}\text{Fe}_{1.6}\text{O}_3$ catalysts.

Catalyst	Temperature (°C)	Degradation (%)	$k(\text{min}^{-1})$	R^2
$\text{La}_{0.2}\text{Mn}_{0.2}\text{Fe}_{1.6}\text{O}_3$	25	85.19	0.0079	0.9955
	35	88.23	0.0089	0.9935
	45	94.87	0.0121	0.9879
	55	90.52	0.0098	0.9869

3.9. Degradation mechanism of dye

The results of dye degradation by using $\text{La}_{0.2}\text{Mn}_{0.2}\text{Fe}_{1.6}\text{O}_3$ as photocatalyst have shown that the dye is being converted into simple harmless components by the action of sunlight. The most probable mechanism to degrade the dyes is shown in Fig. 15. As the sunlight irradiate on the catalytic surface it causes the excitation of electron to produce an electron (e^-) hole (h^+) pair which further degrade the organic dye. The mechanism shows that the excited electrons produced in the conduction band are responsible for the production of super oxide anion radical ($\text{O}_2^{\cdot-}$) which is further converted into hydroperoxyl radical ($\cdot\text{OOH}$) by the reaction with water. In the presence of sunlight this radical rearrange itself to form H_2O_2 . The hydrogen peroxide thus produced reacts with oxygen to produce $\cdot\text{OH}$ [21].

Similarly in the valance band, a reaction between water molecules and holes also takes place and convert it into $\cdot\text{OH}$. These hydroxyl radicals then reacted with organic dye (RhB) and oxidize it into simple harmless substances i.e., CO_2 and H_2O . The results have shown that the synthesized $\text{La}_{0.2}\text{Mn}_{0.2}\text{Fe}_{1.6}\text{O}_3$ nanoparticles have great potential to degrade the organic pollutants.

3.10. Reusability of catalyst

Since the catalyst's stability and durability are crucial factors to consider when considering large-scale industrial applications, four degradation tests were conducted under specific reaction conditions, as shown in Fig. 16. After each cyclic run, the $\text{La}_{0.2}\text{Mn}_{0.2}\text{Fe}_{1.6}\text{O}_3$ catalyst was extracted from the aqueous solution using a magnet, thoroughly washed with deionized water, and dried at 70°C for reuse in the next cycle. When the catalyst is used repeatedly, the degrading efficiency of RhB falls steadily from 91.78 to 85.08%. Photocatalyst aggregation, metal ion leaching, and catalytic site degradation as a result of photocorrosion all contribute to the ultimate loss of catalytic potential. The catalyst used in degradation tests might be recovered in the presence of a high magnetic field. As a result, the reusability experiment anticipates and supports the future use of the $\text{La}_{0.2}\text{Mn}_{0.2}\text{Fe}_{1.6}\text{O}_3$ catalyst for photocatalytic wastewater treatment.

4. Conclusion

The Fe_2O_3 and La-Mn co-doped Fe_2O_3 nanoparticles having a composition of $\text{La}_{0.1}\text{Mn}_{0.3}\text{Fe}_{1.6}\text{O}_3$ and $\text{La}_{0.2}\text{Mn}_{0.2}\text{Fe}_{1.6}\text{O}_3$ were prepared by simple chemical precipitation technique. The SEM and TEM micrographs have revealed the average size of particles is 48.137, 46.923 and 42.861 nm, respectively, and the morphology of the nanoparticles is semi-spherical shaped. These characteristics, along with phase purity and crystalline nature of the nanoparticles, were further confirmed by FTIR and XRD. The zeta potential value for $\text{La}_{0.2}\text{Mn}_{0.2}\text{Fe}_{1.6}\text{O}_3$ is 8.46. The saturation magnetization is 6.17, 3.73 and 2.89 emu/g, respectively. Similarly, the Mr value is 1.15, 0.68 and 0.52 emu/g, respectively. It is observed that doping with Mn and La significantly reduced the particle size, which in turn enhanced the surface area of these synthesized particles. The surface area of undoped and doped particles which was determined by BET is 77.93, 80.23 and 87.45 m^2/g , respectively.

The UV spectrophotometer was used for the measurement of photocatalytic performance of nanoparticles. It was observed from the results that 91.78% RhB dye was degraded in 240 minutes by doping with Mn and La metal ions. Degradation of RhB dye was increased from 43.30 to 89.34% with the increase of pH from 4 to 10 and increased by changing catalytic dosage, dye concentration and temperature. This excellent photodegradation effect of as-synthesized $\text{La}_{0.2}\text{Mn}_{0.2}\text{Fe}_{1.6}\text{O}_3$ nanoparticles revealed that these can be used more effectively for the removal of organic pollutants from sewage water

Declarations

Acknowledgements

We acknowledge to the Institute of Chemistry, The Islamia University of Bahawalpur and Department of Chemistry, The Government Sadiq College Women University Bahawalpur for providing necessary research facilities.

Author Contribution

Sobia maqbool conducted experimental work, data analysis and wrote manuscript. Adeel Ahmad and Arif Mukhtar help in characterizing data. Muhammad Jamshaid help in experimental work. Prof. Dr. Aziz Ur Rehman and Dr. Saima Anjum help out in formulating ideas and research work. All authors read and approved the final manuscript.

Funding

This research did not receive any specific grant from funding agencies in the public, commercial, or not-for-profit sectors.

Ethics approval and consent to participate Not applicable.

Consent for publication Not applicable.

Data availability Not applicable.

Competing interests The authors declare no competing interests.

References

1. Abbas Khaleel M, Parvin M, Al-zamly A (2018) Ti(IV)-doped γ -Fe₂O₃ nanoparticles possessing unique textural and chemical properties: Enhanced suppression of phase transformation and promising catalytic activity. *J Solid State Chem* 259:91–97
2. Ahmad I, Shah SM, Ashiq MN, Khan RA (2016) Effect of Nd³⁺ and Cd²⁺ ions co-substitution on the dielectric and electron transport properties of spinel strontium nanoferrites. *Ceram Int* 42(11):12763–12770. doi: <https://doi.org/10.1016/j.ceramint.2016.05.034>

3. Ahmed A, Usman M, Liu Q-Y, Shen Y-Q, Yu B, Cong H-L (2019) Plant mediated synthesis of copper nanoparticles by using Camellia sinensis leaves extract and their applications in dye degradation. *Ferroelectrics* 549(1):61–69. doi: 10.1080/00150193.2019.1592544
4. Ahmed A, Usman M, Wang S, Yu B, Shen Y, Cong H (2021) Facile synthesis of Zr₄₊ substituted Mn_{0.2}Co_{0.8}Fe_{2-x}O₄ nanoparticles and their composites with reduced graphene oxide for enhanced photocatalytic performance under visible light irradiation. *Synth Met* 277:116766. doi: <https://doi.org/10.1016/j.synthmet.2021.116766>
5. Ahmed A, Usman M, Yu B, Ding X, Peng Q, Shen Y, Cong H (2020) Efficient photocatalytic degradation of toxic Alizarin yellow R dye from industrial wastewater using biosynthesized Fe nanoparticle and study of factors affecting the degradation rate. *J Photochem Photobiol B* 202:111682. doi: <https://doi.org/10.1016/j.jphotobiol.2019.111682>
6. Ahmed A, Usman M, Yu B, Gao F, Shen Y, Cong H (2021) Heterogeneous activation of peroxymonosulfate using superparamagnetic β-CD-CoFe₂O₄ catalyst for the removal of endocrine-disrupting bisphenol A: Performance and degradation mechanism. *Sep Purif Technol* 279:119752. doi: <https://doi.org/10.1016/j.seppur.2021.119752>
7. Ahmed A, Usman M, Yu B, Shen Y, Cong H (2021) Sustainable fabrication of hematite (α-Fe₂O₃) nanoparticles using biomolecules of Punica granatum seed extract for unconventional solar-light-driven photocatalytic remediation of organic dyes. *J Mol Liq* 339:116729. doi: <https://doi.org/10.1016/j.molliq.2021.116729>
8. Almeida WLd, Rodembusch FS, Ferreira NS, Caldas de Sousa V (2020) Eco-friendly and cost-effective synthesis of ZnO nanopowders by Tapioca-assisted sol-gel route. *Ceramics International*, 46(8, Part A), 10835–10842. doi: <https://doi.org/10.1016/j.ceramint.2020.01.095>
9. Ashar A, Bhatti IA, Ashraf M, Tahir AA, Aziz H, Yousuf M, Bhutta ZA (2020) Fe³⁺ @ ZnO/polyester based solar photocatalytic membrane reactor for abatement of RB5 dye. *J Clean Prod* 246:119010. doi: <https://doi.org/10.1016/j.jclepro.2019.119010>
10. Baig MM, Zulfiqar S, Yousuf MA, Touqueer M, Ullah S, Agboola P, Shakir I (2020) Structural and photocatalytic properties of new rare earth La₃₊ substituted MnFe₂O₄ ferrite nanoparticles. *Ceram Int* 46(14):23208–23217. doi: <https://doi.org/10.1016/j.ceramint.2020.06.103>
11. Bibi I, Kamal S, Ahmed A, Iqbal M, Nouren S, Jilani K, Majid F (2017) Nickel nanoparticle synthesis using Camellia Sinensis as reducing and capping agent: Growth mechanism and photo-catalytic activity evaluation. *Int J Biol Macromol* 103:783–790. doi: <https://doi.org/10.1016/j.ijbiomac.2017.05.023>
12. Bouhjar F, Derbali L, Marić B, Bessaï's B (2020) Electrodeposited Cr-Doped α-Fe₂O₃ thin films active for photoelectrochemical water splitting. *Int J Hydrog Energy* 45:11492–11501. doi: <https://doi.org/10.1016/j.ijhydene.2019.10.215>
13. Chen G, Zhang X, Gao Y, Zhu G, Cheng Q, Cheng X (2019) Novel magnetic MnO₂/MnFe₂O₄ nanocomposite as a heterogeneous catalyst for activation of peroxymonosulfate (PMS) toward

oxidation of organic pollutants. Sep Purif Technol 213:456–464. doi:

<https://doi.org/10.1016/j.seppur.2018.12.049>

14. Chowdhury A, Khan AA, Kumari S, Hussain S (2019) Superadsorbent Ni–Co–S/SDS Nanocomposites for Ultrahigh Removal of Cationic, Anionic Organic Dyes and Toxic Metal Ions: Kinetics, Isotherm and Adsorption Mechanism. ACS Sustain Chem Eng 7(4):4165–4176. doi: 10.1021/acssuschemeng.8b05775
15. Das S, Mahalingam H (2020) Novel immobilized ternary photocatalytic polymer film based airlift reactor for efficient degradation of complex phthalocyanine dye wastewater. J Hazard Mater 383:121219. doi: <https://doi.org/10.1016/j.jhazmat.2019.121219>
16. Demirci S, Yurddaskal M, Dikici T, Sarıoğlu C (2018) Fabrication and characterization of novel iodine doped hollow and mesoporous hematite (Fe₂O₃) particles derived from sol-gel method and their photocatalytic performances. J Hazard Mater 345:27–37. doi: <https://doi.org/10.1016/j.jhazmat.2017.11.009>
17. Dinesh GK, Pramod M, Chakma S (2020) Sonochemical synthesis of amphoteric CuO-Nanoparticles using Hibiscus rosa-sinensis extract and their applications for degradation of 5-fluorouracil and lovastatin drugs. J Hazard Mater 399:123035. doi: <https://doi.org/10.1016/j.jhazmat.2020.123035>
18. Duan Q, Ji J, Hong X, Fu Y, Wang C, Zhou K, Wang Z-Y (2020) Design of hole-transport-material free CH₃NH₃PbI₃/CsSnI₃ all-perovskite heterojunction efficient solar cells by device simulation. Sol Energy 201:555–560. doi: <https://doi.org/10.1016/j.solener.2020.03.037>
19. Feriel Bouhjar L, Derbali, Bessaïs B (2020) Electrodeposited Cr-Doped α-Fe₂O₃ thin films active for photoelectrochemical water splitting. *international journal of hydrogen energy*, 45 11492–11501
20. Gao H, Zhao X, Zhang H, Chen J, Wang S, Yang H (2020) Construction of 2D/0D/2D Face-to-Face Contact g-C₃N₄@Au@Bi₄Ti₃O₁₂ Heterojunction Photocatalysts for Degradation of Rhodamine B. J Electron Mater 49(9):5248–5259. doi: 10.1007/s11664-020-08243-2
21. Guo S, Wang H, Yang W, Fida H, You L, Zhou K (2020) Scalable synthesis of Ca-doped α-Fe₂O₃ with abundant oxygen vacancies for enhanced degradation of organic pollutants through peroxyomonosulfate activation. Appl Catal B 262:118250. doi: <https://doi.org/10.1016/j.apcatb.2019.118250>
22. Guo W, Sun W, Lv LP, Kong S, Wang Y (2017) Microwave-assisted morphology evolution of Fe-based metal-organic frameworks and their derived Fe₂O₃ nanostructures for Li-ion storage. ACS Nano 11:4198–4205. doi: <https://doi.org/10.1021/acsnano.7b01152>
23. Harish KN, Naik B, Prashanth kumar HS, Viswanath R (2013) Optical and Photocatalytic Properties of Solar Light Active Nd-Substituted Ni Ferrite Catalysts: For Environmental Protection. ACS Sustain Chem Eng 1(9):1143–1153. doi: 10.1021/sc400060z
24. Khodadadi B, Bordbar M, Nasrollahzadeh M (2017) Green synthesis of Pd nanoparticles at Apricot kernel shell substrate using Salvia hydrangea extract: Catalytic activity for reduction of organic dyes. J Colloid Interface Sci 490:1–10. doi: <https://doi.org/10.1016/j.jcis.2016.11.032>

25. Kumar A, Sharma G, Naushad M, Al-Muhtaseb AaH, García-Peñas A, Mola GT, Stadler FJ (2020) Bio-inspired and biomaterials-based hybrid photocatalysts for environmental detoxification: A review. *Chem Eng J* 382:122937. doi: <https://doi.org/10.1016/j.cej.2019.122937>
26. Lim Y-F, Chua CS, Lee CJ, Chi D (2014) Sol-gel deposited Cu₂O and CuO thin films for photocatalytic water splitting. *Phys Chem Chem Phys* 16(47):25928–25934. doi: 10.1039/C4CP03241A
27. Liu J, Li J, Wei F, Zhao X, Su Y, Han X (2019) Ag-ZnO Submicrometer Rod Arrays for High-Efficiency Photocatalytic Degradation of Congo Red and Disinfection. *ACS Sustain Chem Eng* 7(13):11258–11266. doi: 10.1021/acssuschemeng.9b00610
28. Lv S-W, Liu J-M, Zhao N, Li C-Y, Wang Z-H, Wang S (2020) Benzothiadiazole functionalized Co-doped MIL-53-NH₂ with electron deficient units for enhanced photocatalytic degradation of bisphenol A and ofloxacin under visible light. *J Hazard Mater* 387:122011. doi: <https://doi.org/10.1016/j.jhazmat.2019.122011>
29. Ma J, Chen K (2018) Silica-free hydrothermal synthesis of ε-Fe₂O₃ nanoparticles and their oriented attachment to nanoflakes with unique magnetism evolution. *Ceram Int* 44(16):19338–19344. doi: <https://doi.org/10.1016/j.ceramint.2018.07.162>
30. Martínez-López S, Lucas-Abellán C, Serrano-Martínez A, Mercader-Ros MT, Cuartero N, Navarro P, Gómez-López VM (2019) Pulsed light for a cleaner dyeing industry: Azo dye degradation by an advanced oxidation process driven by pulsed light. *J Clean Prod* 217:757–766. doi: <https://doi.org/10.1016/j.jclepro.2019.01.230>
31. Mengying S, Cheng YuLHao, Ma J, Qin Y, Kong Y, Komarneni S (2020) Mg doped CuO-Fe₂O₃ composites activated by persulfate as highly active heterogeneous catalysts for the degradation of organic pollutants. *J Alloys Compd* 825:154036
32. Mengying S, Cheng YuLHao, Ma J, Qin Y, Kong Y, Komarneni S (2020) Mg doped CuOeFe₂O₃ composites activated by persulfate as highly active heterogeneous catalysts for the degradation of organic pollutants. *Journal of Alloys and Compounds*, 825
33. Mostafa MH, Elsawy MA, Darwish MSA, Hussein LI, Abdaleem AH (2020) Microwave-Assisted preparation of Chitosan/ZnO nanocomposite and its application in dye removal. *Mater Chem Phys* 248:122914. doi: <https://doi.org/10.1016/j.matchemphys.2020.122914>
34. Ndagijimana P, Liu X, Li Z, Yu G, Wang Y (2019) Optimized synthesis of a core-shell structure activated carbon and its adsorption performance for Bisphenol A. *Sci Total Environ* 689:457–468. doi: <https://doi.org/10.1016/j.scitotenv.2019.06.235>
35. Park JH, Ahn HS (2020) Electrochemical synthesis of multimetallic nanoparticles and their application in alkaline oxygen reduction catalysis. *Appl Surf Sci* 504:144517. doi: <https://doi.org/10.1016/j.apsusc.2019.144517>
36. Payra S, Challagulla S, Bobde Y, Chakraborty C, Ghosh B, Roy S (2019) Probing the photo- and electro-catalytic degradation mechanism of methylene blue dye over ZIF-derived ZnO. *J Hazard Mater* 373:377–388. doi: <https://doi.org/10.1016/j.jhazmat.2019.03.053>

37. Peng K, Fu L, Yang H, Ouyang J (2016) Perovskite LaFeO₃/montmorillonite nanocomposites: synthesis, interface characteristics and enhanced photocatalytic activity. *Sci Rep* 6(1):19723. doi: 10.1038/srep19723
38. Popov N, Krehula S, Ristić M, Kuzmann E, Homonnay Z, Bošković M, Musić S (2021) Influence of Cr doping on the structural, magnetic, optical and photocatalytic properties of α-Fe₂O₃ nanorods. *J Phys Chem Solids* 148:109699. doi: <https://doi.org/10.1016/j.jpcs.2020.109699>
39. Suresh R, Giribabu K, Manigandan R, Mangalaraja RV, Solorza JY, Stephen A, Professor VNA (2017) Synthesis of Co₂β-doped Fe₂O₃ photocatalyst for degradation of pararosaniline dye. *Solid State Sci* 68:39–46
40. Rashmi SK, Naik B, Jayadevappa HS, Viswanath H, Patil R, Naik M, M (2017) Solar light responsive Sm-Zn ferrite nanoparticle as efficient photocatalyst. *Mater Sci Engineering: B* 225:86–97. doi: <https://doi.org/10.1016/j.mseb.2017.08.012>
41. Raza N, Raza W, Gul H, Azam M, Lee J, Vikrant K, Kim K-H (2020) Solar-light-active silver phosphate/titanium dioxide/silica heterostructures for photocatalytic removal of organic dye. *J Clean Prod* 254:120031. doi: <https://doi.org/10.1016/j.jclepro.2020.120031>
42. Reddy IN, Reddy CV, Sreedhar A, Cho M, Kim D, Shim J (2019) Effect of plasmonic Ag nanowires on the photocatalytic activity of Cu doped Fe₂O₃ nanostructures photoanodes for superior photoelectrochemical water splitting applications. *J Electroanal Chem* 842:146–160. doi: <https://doi.org/10.1016/j.jelechem.2019.04.076>
43. Ritika, Kaur M, Umar A, Mehta SK, Kansal SK (2019) BiF₃ octahedrons: A potential natural solar light active photocatalyst for the degradation of Rhodamine B dye in aqueous phase. *Mater Res Bull* 112:376–383. doi: <https://doi.org/10.1016/j.materresbull.2018.12.031>
44. Rojas S, Horcajada P (2020) Metal–Organic Frameworks for the Removal of Emerging Organic Contaminants in Water. *Chem Rev* 120(16):8378–8415. doi: 10.1021/acs.chemrev.9b00797
45. Sharifi I, Shokrollahi H, Amiri S (2012) Ferrite-based magnetic nanofluids used in hyperthermia applications. *J Magn Magn Mater* 324(6):903–915. doi: <https://doi.org/10.1016/j.jmmm.2011.10.017>
46. Selvin SP, Ganesh Kumar S, Sarala A, Rajaram L, Sathiyan R, Princy Merlin A, Lydia S, I (2018) Photocatalytic Degradation of Rhodamine B Using Zinc Oxide Activated Charcoal Polyaniline Nanocomposite and Its Survival Assessment Using Aquatic Animal Model. *ACS Sustain Chem Eng* 6(1):258–267. doi: 10.1021/acssuschemeng.7b02335
47. Sun M, Lei Y, Cheng H, Ma J, Qin Y, Kong Y, Komarneni S (2020) Mg doped CuO–Fe₂O₃ composites activated by persulfate as highly active heterogeneous catalysts for the degradation of organic pollutants. *J Alloys Compd* 825:154036. doi: <https://doi.org/10.1016/j.jallcom.2020.154036>
48. Tang Y, He D, Guo Y, Qu W, Shang J, Zhou L, Dong W (2020) Electrochemical oxidative degradation of X-6G dye by boron-doped diamond anodes: Effect of operating parameters. *Chemosphere* 258:127368. doi: <https://doi.org/10.1016/j.chemosphere.2020.127368>

49. Usman M, Ahmed A, Yu B, Peng Q, Shen Y, Cong H (2019) Photocatalytic potential of bio-engineered copper nanoparticles synthesized from *Ficus carica* extract for the degradation of toxic organic dye from waste water: Growth mechanism and study of parameter affecting the degradation performance. *Mater Res Bull* 120:110583. doi: <https://doi.org/10.1016/j.materresbull.2019.110583>
50. Usman M, Ahmed A, Yu B, Wang S, Shen Y, Cong H (2021) Simultaneous adsorption of heavy metals and organic dyes by β -Cyclodextrin-Chitosan based cross-linked adsorbent. *Carbohydr Polym* 255:117486. doi: <https://doi.org/10.1016/j.carbpol.2020.117486>
51. Wang N, Han B, Wen J, Liu M, Li X (2019) Synthesis of novel Mn-doped Fe₂O₃ nanocube supported g-C₃N₄ photocatalyst for overall visible-light driven water splitting. *Colloids Surf A* 567:313–318. doi: <https://doi.org/10.1016/j.colsurfa.2019.01.053>
52. Wang T, Can I, Zhang S, He J, Sun P, Liu F, Lu G (2018) Self-Assembly Template Driven 3D Inverse Opal Microspheres Functionalized with Catalyst Nanoparticles Enabling a Highly Efficient Chemical Sensing Platform. *ACS Appl Mater Interfaces* 10(6):5835–5844. doi: 10.1021/acsami.7b19641
53. Wu H, Wu X-L, Mine S, Matsuoka M, Chu Y-H, Wang Z-M (2020) Crafting carbon sphere-titania core-shell interfacial structure to achieve enhanced visible light photocatalysis. *Appl Surf Sci* 534:147566. doi: <https://doi.org/10.1016/j.apsusc.2020.147566>
54. Xu H-M, Sun X-F, Wang S-Y, Song C, Wang S-G (2018) Development of laccase/graphene oxide membrane for enhanced synthetic dyes separation and degradation. *Sep Purif Technol* 204:255–260. doi: <https://doi.org/10.1016/j.seppur.2018.04.036>
55. Huang Y, Nengzi Li-chao, Zhang X, Gou J, Gao Y, Zhu G, Cheng X (2020) Catalytic degradation of ciprofloxacin by magnetic CuS/Fe₂O₃/Mn₂O₃ nanocomposite activated peroxymonosulfate: Influence factors, degradation pathways and reaction mechanism. *Chemical Engineering Journal*, 388
56. Yousuf MA, Baig MM, Waseem M, Haider S, Shakir I, Ud-Din Khan S, Warsi MF (2019) Low cost micro-emulsion route synthesis of Cr-substituted MnFe₂O₄ nanoparticles. *Ceram Int* 45:22316–22323 17, Part. doi: <https://doi.org/10.1016/j.ceramint.2019.07.259>
57. Zare M, Namratha K, Thakur MS, Byrappa K (2019) Biocompatibility assessment and photocatalytic activity of bio-hydrothermal synthesis of ZnO nanoparticles by *Thymus vulgaris* leaf extract. *Mater Res Bull* 109:49–59. doi: <https://doi.org/10.1016/j.materresbull.2018.09.025>
58. Zheng X, Zhang Z, Meng S, Wang Y, Li D (2020) Regulating charge transfer over 3D Au/ZnO hybrid inverse opal toward efficiently photocatalytic degradation of bisphenol A and photoelectrochemical water splitting. *Chem Eng J* 393:124676. doi: <https://doi.org/10.1016/j.cej.2020.124676>
59. Zhou X, Zhu Y, Luo W, Ren Y, Xu P, Elzatahry AA, Zhao D (2016) Chelation-assisted soft-template synthesis of ordered mesoporous zinc oxides for low concentration gas sensing. *J Mater Chem A* 4(39):15064–15071. doi: 10.1039/C6TA05687C
60. Zinatloo-Ajabshir S, Salehi Z, Salavati-Niasari M (2018) Green synthesis and characterization of Dy₂Ce₂O₇ nanostructures using *Ananas comosus* with high visible-light photocatalytic activity of

Figures

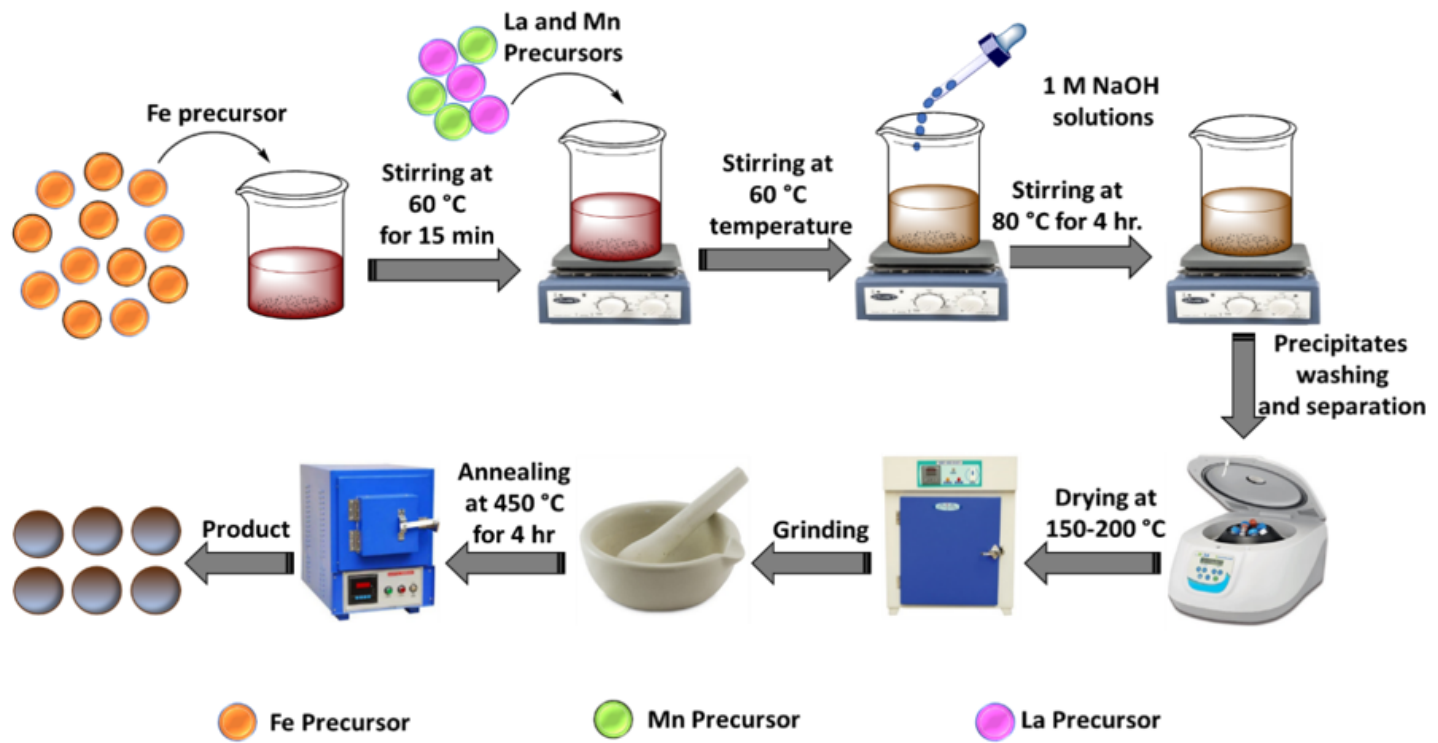


Figure 1

Schematic diagram for the preparation of La-Mn co-doped Fe_2O_3 nanoparticles.

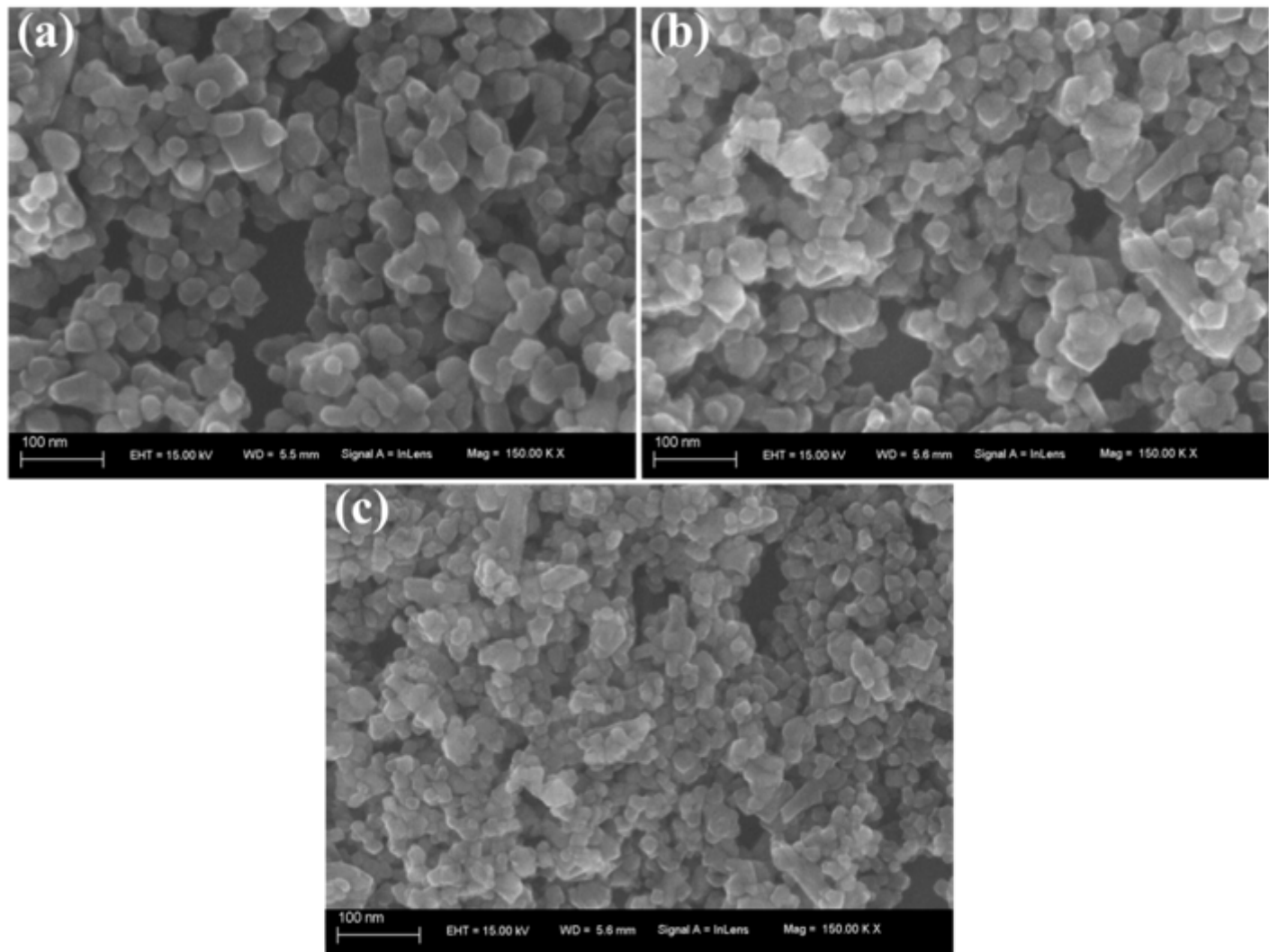


Figure 2

SEM Micrographs of (a) Fe_2O_3 , (b) $\text{La}_{0.1}\text{Mn}_{0.3}\text{Fe}_{1.6}\text{O}_3$ and (c) $\text{La}_{0.2}\text{Mn}_{0.2}\text{Fe}_{1.6}\text{O}_3$.

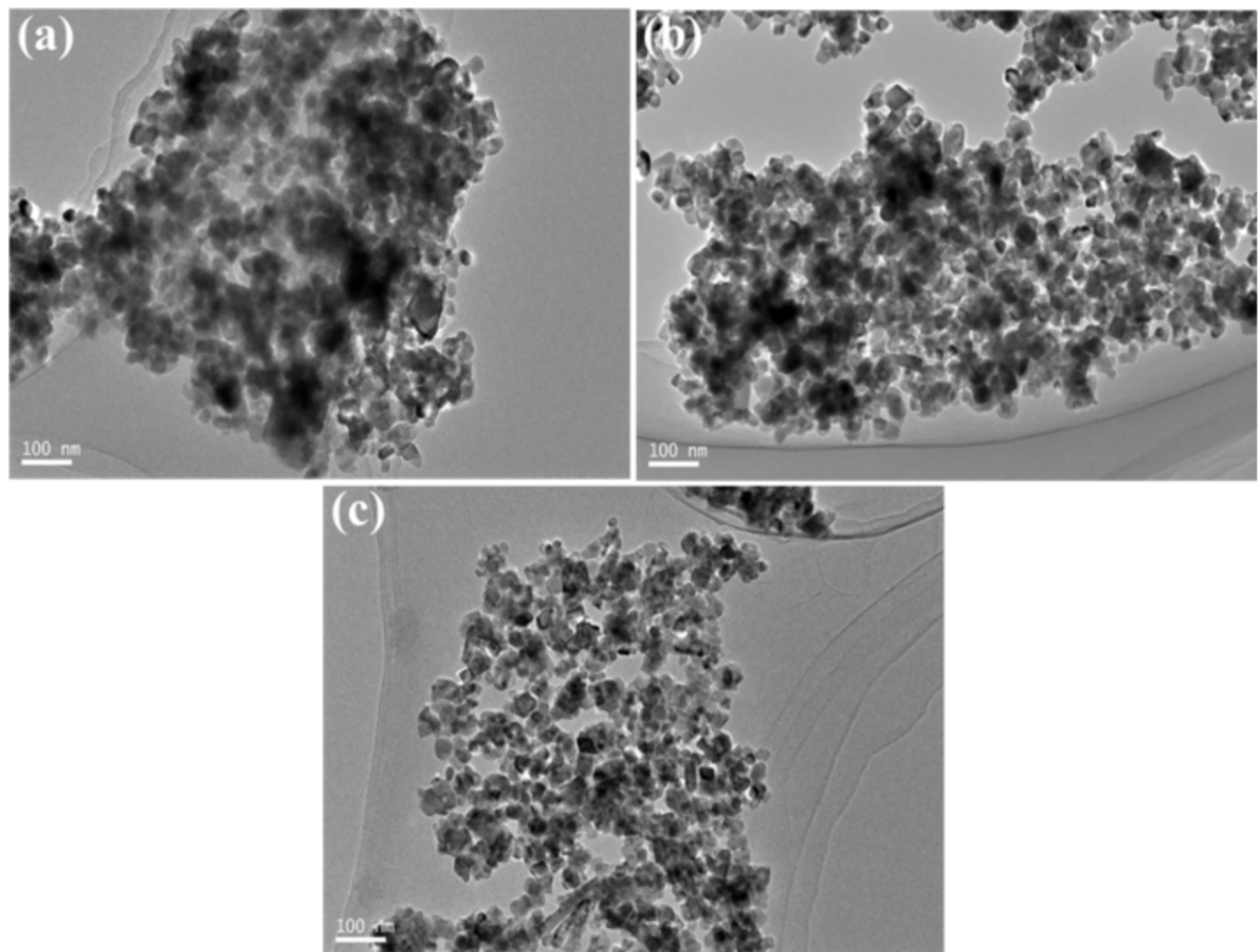


Figure 3

TEM Micrographs of (a) Fe_2O_3 , (b) $\text{La}_{0.1}\text{Mn}_{0.3}\text{Fe}_{1.6}\text{O}_3$ and (c) $\text{La}_{0.2}\text{Mn}_{0.2}\text{Fe}_{1.6}\text{O}_3$.

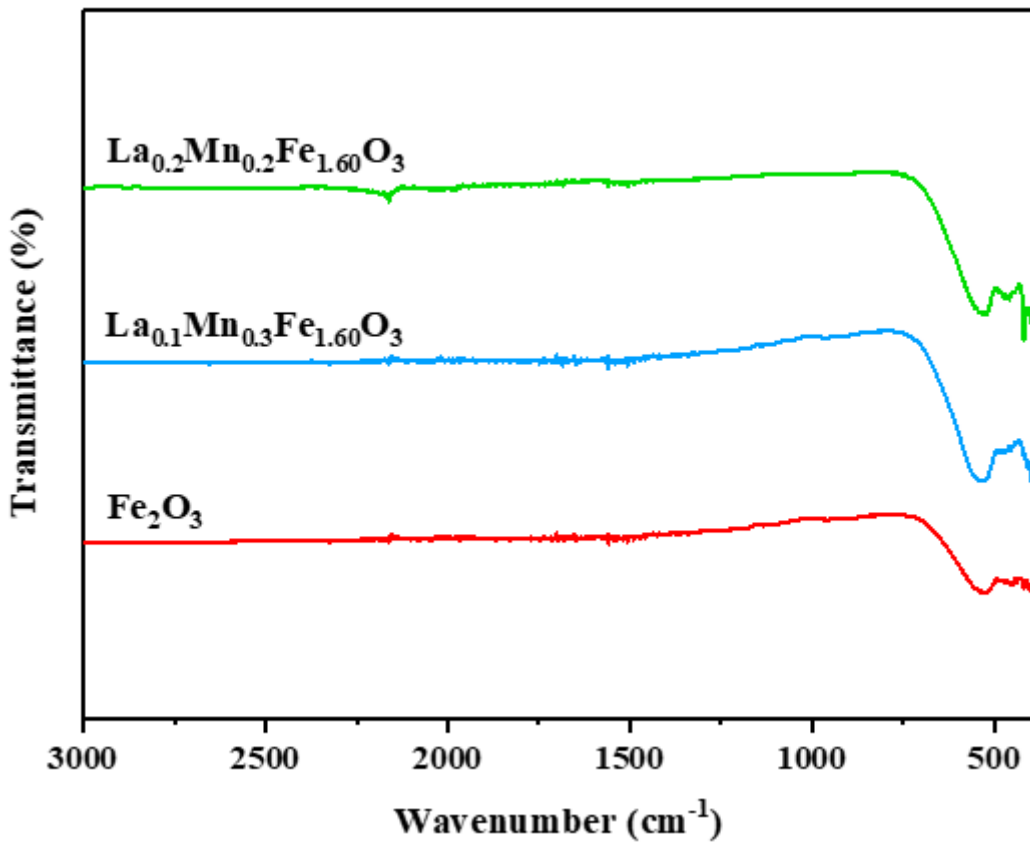


Figure 4

FTIR analysis of Fe_2O_3 , $\text{La}_{0.1}\text{Mn}_{0.3}\text{Fe}_{1.6}\text{O}_3$ and $\text{La}_{0.2}\text{Mn}_{0.2}\text{Fe}_{1.6}\text{O}_3$ nanoparticles.

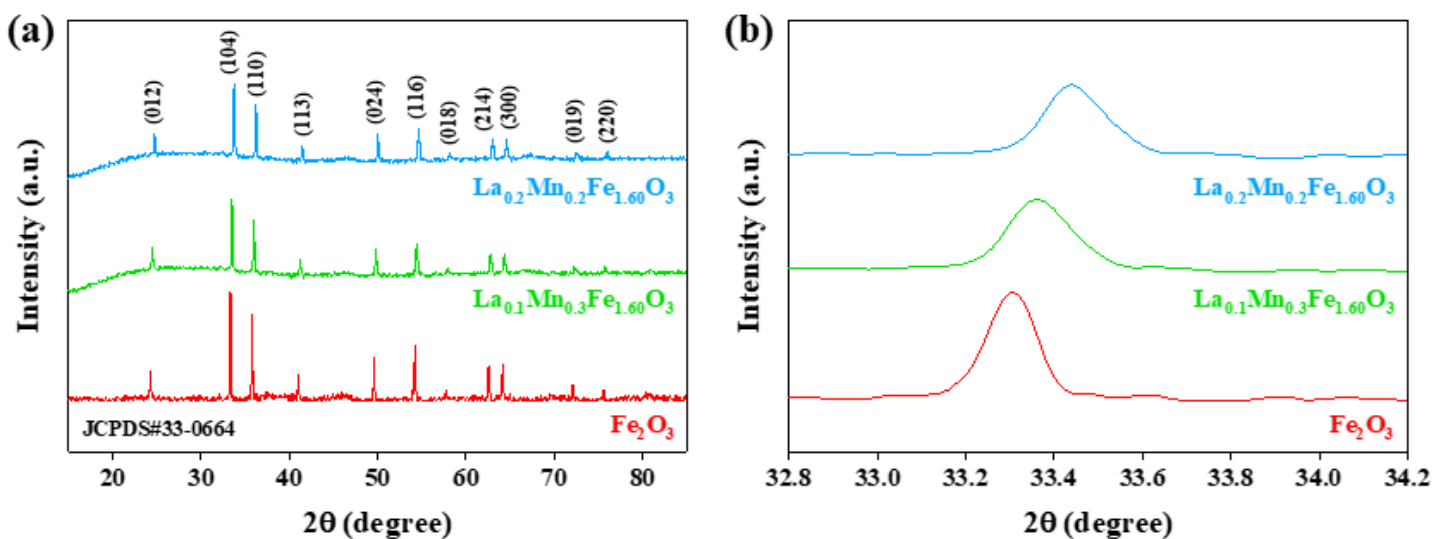


Figure 5

XRD pattern of Fe_2O_3 nanoparticles, $\text{La}_{0.1}\text{Mn}_{0.3}\text{Fe}_{1.6}\text{O}_3$ and $\text{La}_{0.2}\text{Mn}_{0.2}\text{Fe}_{1.6}\text{O}_3$ nanoparticles.

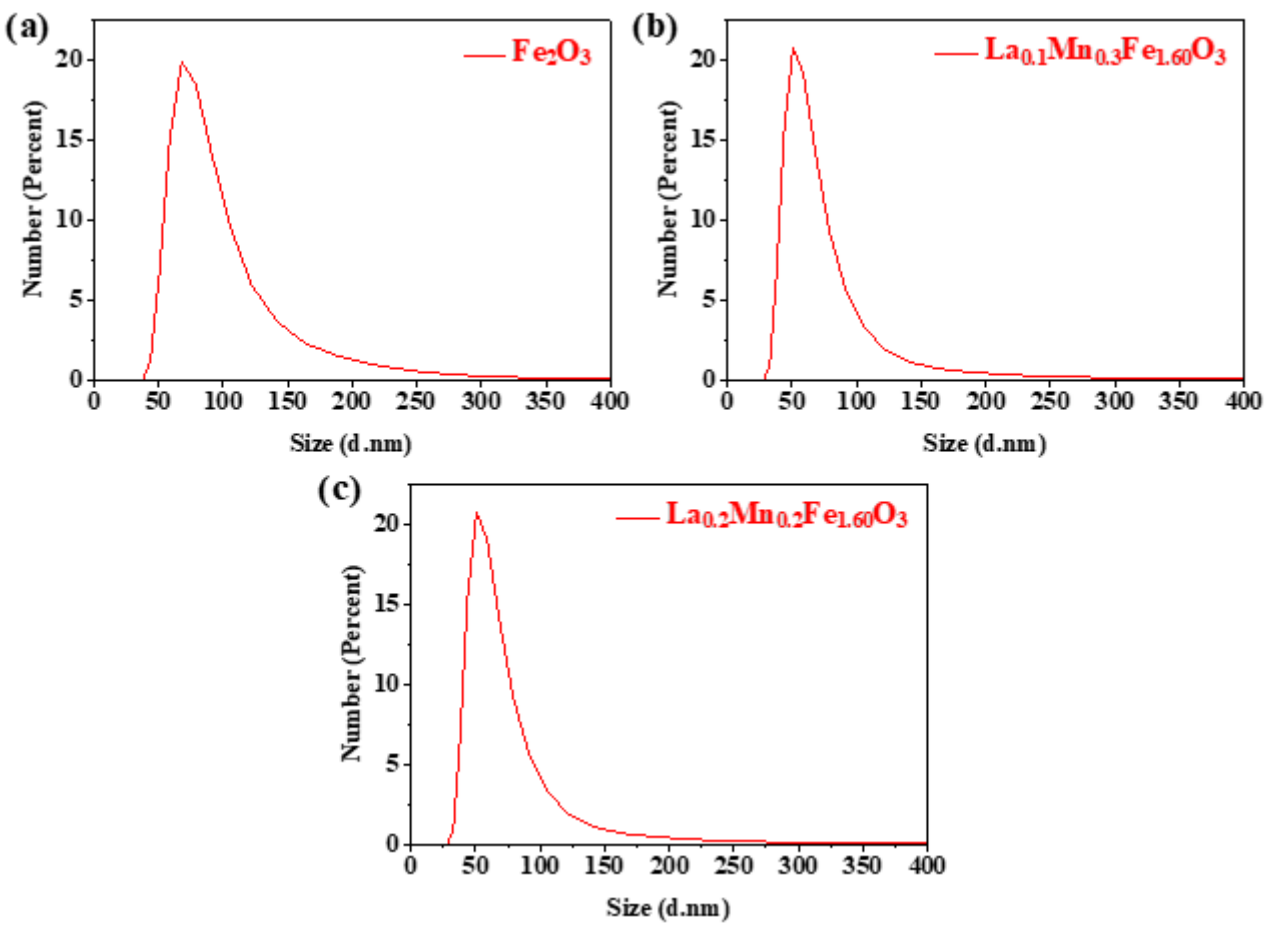


Figure 6

DLS size measurements of (a) Fe_2O_3 , (b) $\text{La}_{0.1}\text{Mn}_{0.3}\text{Fe}_{1.6}\text{O}_3$, and (c) $\text{La}_{0.2}\text{Mn}_{0.2}\text{Fe}_{1.6}\text{O}_3$ nanoparticles.

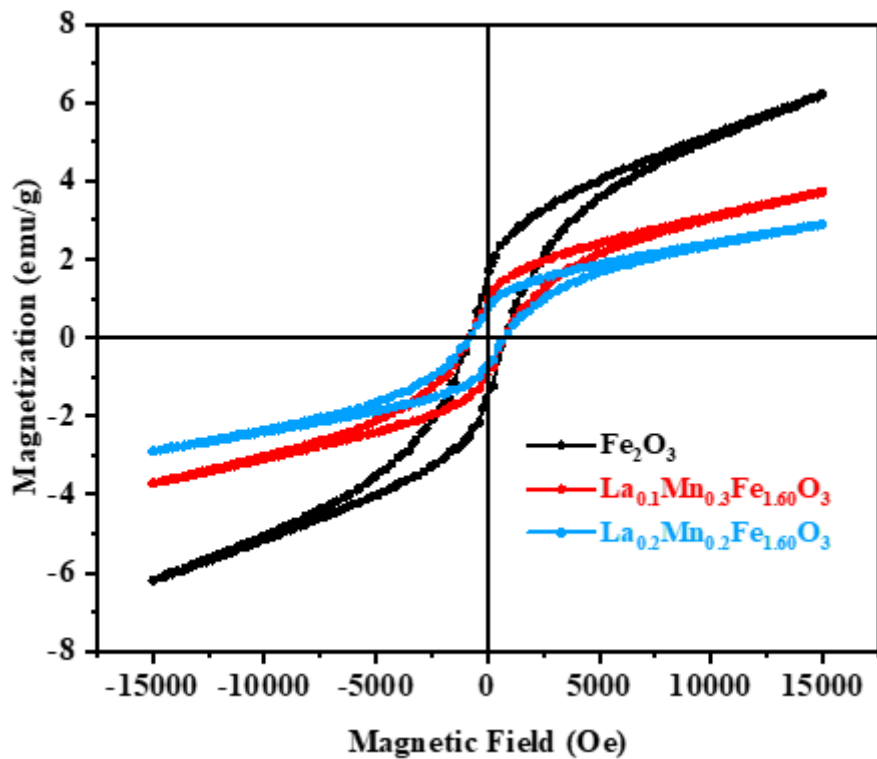


Figure 7

M-H loops of Fe_2O_3 , $\text{La}_{0.1}\text{Mn}_{0.3}\text{Fe}_{1.6}\text{O}_3$ and $\text{La}_{0.2}\text{Mn}_{0.2}\text{Fe}_{1.6}\text{O}_3$.

Figure 8

N_2 Adsorption-desorption isotherm of (a) Fe_2O_3 , (b) $\text{La}_{0.1}\text{Mn}_{0.3}\text{Fe}_{1.6}\text{O}_3$ and (c) $\text{La}_{0.2}\text{Mn}_{0.2}\text{Fe}_{1.6}\text{O}_3$.

Figure 9

(a) Absorption spectra of RhB dye solution at different time intervals using Fe_2O_3 nanoparticles, (b) $\text{La}_{0.1}\text{Mn}_{0.3}\text{Fe}_{1.6}\text{O}_3$ nanoparticles, (c) $\text{La}_{0.2}\text{Mn}_{0.2}\text{Fe}_{1.6}\text{O}_3$ nanoparticles.

Figure 10

Isoelectric point of $\text{La}_{0.2}\text{Mn}_{0.2}\text{Fe}_{1.6}\text{O}_3$ catalyst.

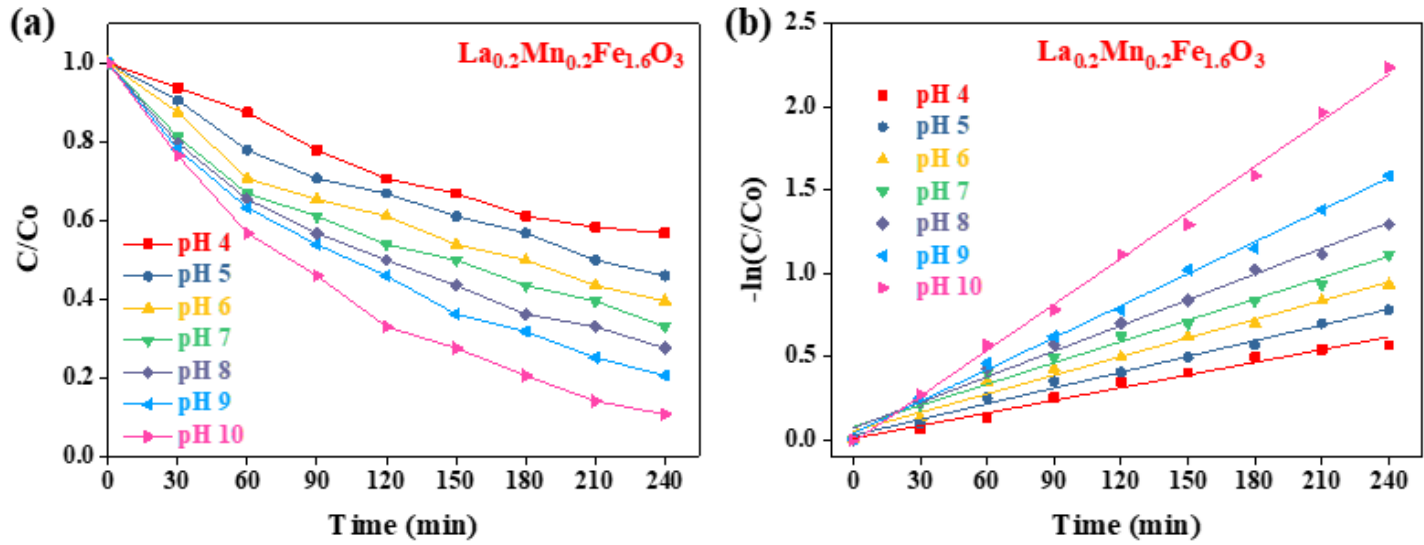


Figure 11

Photocatalytic degradation of RhB dye at different pH conditions; (a) degradation rate of RhB, (b) kinetic plot for RhB. Conditions; $[(\text{RhB}) = 50 \text{ ppm}; (\text{catalyst}) = 40 \text{ mg/L}; \text{pH} = 4-10; T = 25^\circ\text{C}]$.

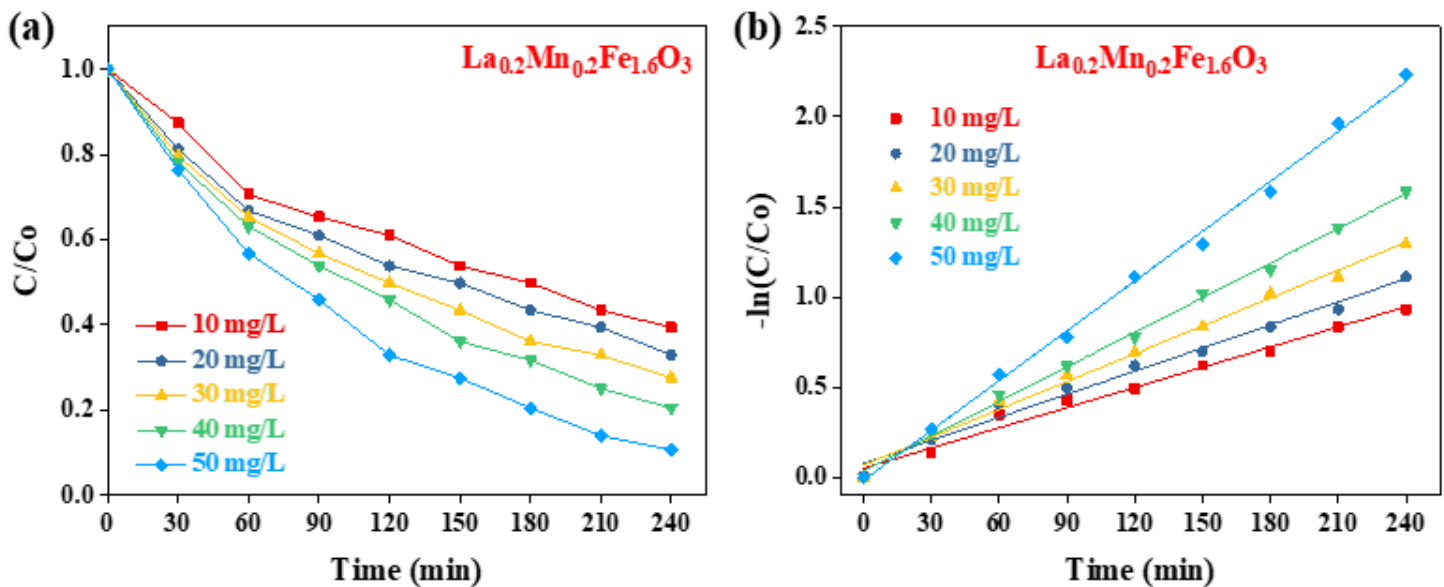


Figure 12

Photocatalytic degradation of RhB dye at different catalyst dosage; (a) degradation rate of RhB, (b) kinetic plot for RhB. Conditions; $[(\text{RhB}) = 50 \text{ ppm}; [\text{catalyst}] = 10-50 \text{ mg/L}; \text{pH} = 7.0; T = 25^\circ\text{C}]$.

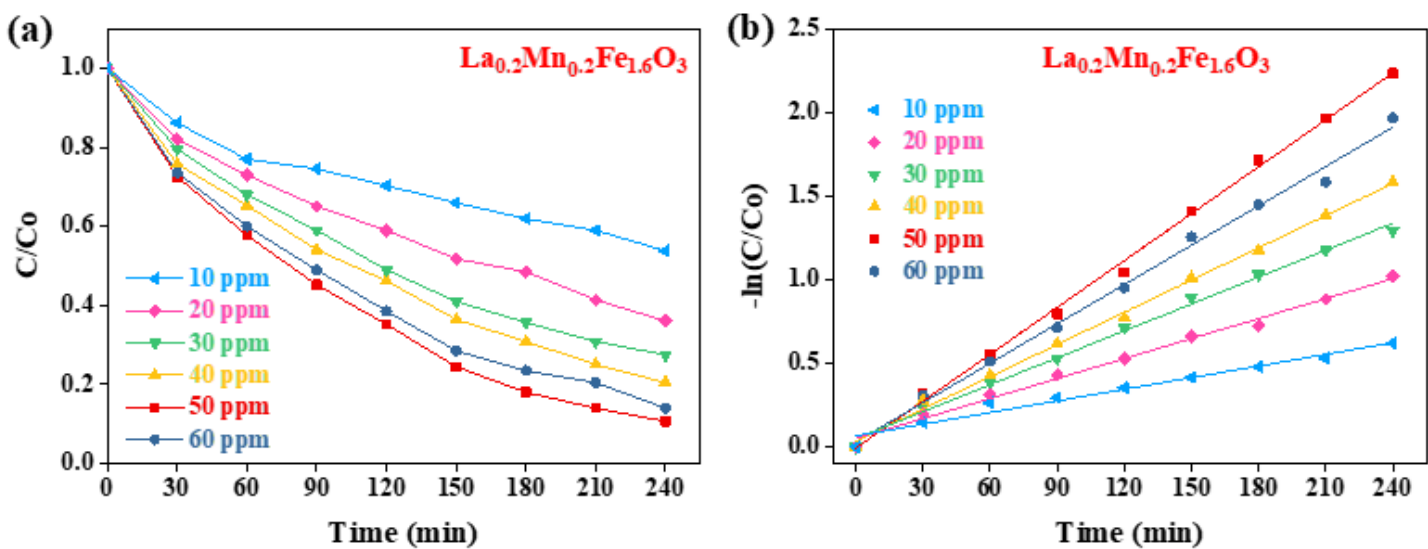


Figure 13

Photocatalytic degradation of RhB dye at different initial dye concentrations; (a) degradation rate of RhB, (b) kinetic plot for RhB. Conditions; ($[\text{RhB}] = 10\text{-}60 \text{ ppm}$; $[\text{catalyst}] = 40 \text{ mg/L}$; $\text{pH} = 7.0$; $T = 25^\circ\text{C}$).

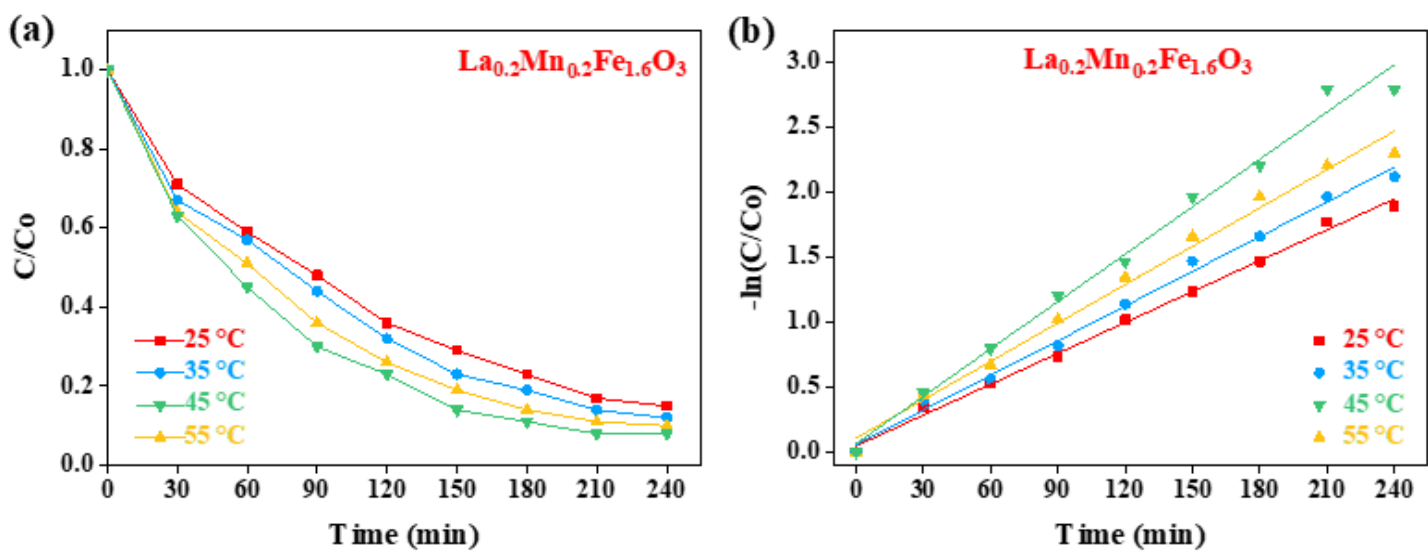


Figure 14

Photocatalytic degradation of RhB dye at different temperature conditions; (a) degradation rate of RhB, (b) kinetic plot for RhB. Conditions; ($[\text{RhB}] = 50 \text{ ppm}$; $[\text{catalyst}] = 40 \text{ mg/L}$; $\text{pH} = 7$; $T = 25\text{-}55^\circ\text{C}$).

Figure 15

Proposed mechanism of RhB dye degradation by using $\text{La}_{0.2}\text{Mn}_{0.2}\text{Fe}_{1.6}\text{O}_3$ nanoparticles.

Figure 16

Reusability of $\text{La}_{0.2}\text{Mn}_{0.2}\text{Fe}_{1.6}\text{O}_3$ nanoparticles for RhB dye degradation.